Supporting Information: Graphene BioFET sensors for SARS-CoV-2 detection: A multiscale approach

A. Toral-Lopez,[1, a)] D.B. Kokh,[2] E.G. Marin,[1] R.C. Wade,[2, 3, 4] and A. Godoy[1]
[1)] *Departamento de Electrónica y Tecnología de Computadores, Facultad de Ciencias, Universidad de Granada (Spain)*
[2)] *Molecular and Cellular Modeling Group, Heidelberg Institute for Theoretical Studies, Schloss-Wolfsbrunnenweg 35, 69118 Heidelberg, Germany*
[3)] *Center for Molecular Biology (ZMBH), DKFZ-ZMBH Alliance, Heidelberg University, Im Neuenheimer Feld 282, 69120 Heidelberg, Germany*
[4)] *Interdisciplinary Center for Scientific Computing (IWR), Heidelberg University, Im Neuenheimer Feld 205, Heidelberg, Germany*

(Dated: 9 March 2022)

SUPPORTING NOTE 1: SELF-CONSISTENT GRAPHENE-BASED BIOFET SENSOR SIMULATION

The numerical description of the Graphene BioFET is based on the solution of the Poisson equation in combination with the continuity equation for electrons and holes along the semiconductor channel. A self-consistent scheme is implemented to solve this set of equations in a two-dimensional cross-section of the structure that allows us to evaluate the charge distribution in their different regions.

In the graphene channel the continuity equation is solved in the diffusive regime assuming a common Fermi level (E_{F}) for both electrons and holes[1–3]. E_{F} jointly with the DoS are used to evaluate the electron and hole density along the graphene channel and then the source-drain current according to the expression:

$$I_{\mathrm{DS}} = q\left(n\mu_{\mathrm{n}} + p\mu_{\mathrm{p}}\right)\nabla V_{\mathrm{E_F}} \tag{1}$$

where q is the elementary charge, $V_{\mathrm{E_F}}$ is the Fermi level potential ($E_{\mathrm{F}} = -qV_{\mathrm{E_F}}$), n (p) is the electron (hole) density and μ_{n} (μ_{p}) the electron (hole) mobility. The latter parameter includes longitudinal-electric field ($|\mathbf{E}_{\mathrm{x}}|$) dependencies and velocity saturation (v_{sat}) effects[4]:

$$\mu = \frac{\mu_0}{\left[1 + \left(|\mathbf{E}_{\mathrm{x}}|\frac{\mu_0}{v_{\mathrm{sat}}}\right)^{\beta}\right]^{1/\beta}} \tag{2}$$

For the electrolyte region we solve the modified Poisson-Boltzmann equation[5] that includes steric effects (a limitation in the concentration due to the finite size of ions) in the distribution of the i-th ion:

$$c_i = c_{i,0}\frac{\mathrm{e}^{qz_i(V-V_{\mathrm{Ref}})/(k_{\mathrm{B}}T)}\mathrm{e}^{-V_{\mathrm{PMF},i}}}{1 - 2\frac{c_{i,0}}{c_{\mathrm{max},i}}\left(1 - \cosh\left(q|z_i|\frac{V-V_{\mathrm{Ref}}}{k_{\mathrm{B}}T}\right)\right)} \tag{3}$$

where, $c_{i,0}$ is the bulk concentration, $c_{\mathrm{max},i}$ the maximum allowed concentration, z_i the ion valence and $V_{\mathrm{PMF},i}$ the Potentials of Mean Force profile. The latter is an additional element that includes the interactions at the electrolyte-solid interface. The value of these profiles are extracted from references[6,7] where Molecular Dynamics simulations were carried out to evaluate the interactions for different types of ions. As a result, they provide a set of distance-to-surface dependent profiles. These came along with a variable water permittivity ε_{w} profile associated to a position dependent water density. In order to prevent unrealistic hydrogen and hydroxyl ion concentrations, PMF profiles for these ions are considered in accordance with the aforementioned water density profiles. We define exponential PMF profiles that result in a negligible concentration below the position of the Gibbs dividing surface reported by[6,7].

In addition to the potential dependent model for the distribution of ions, we also include the reactions involving the components of the Phosphate Buffer (PBS) following[8]. This is only considered for the elements that constitute

[a)] Electronic mail: atoral@ugr.es

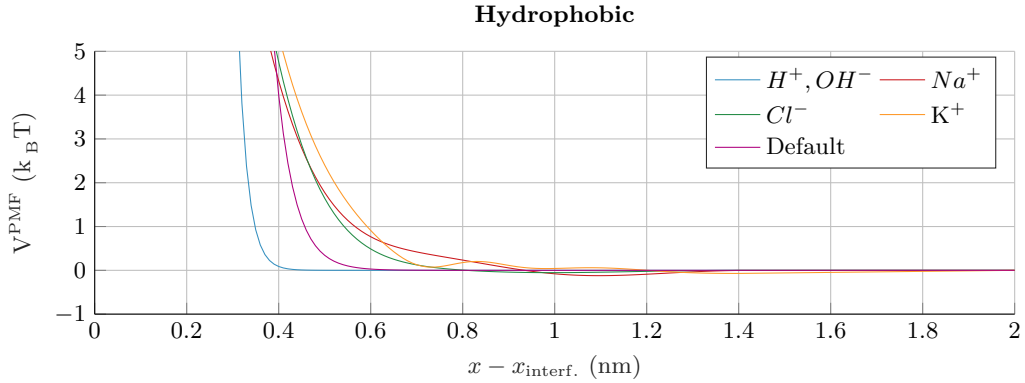

FIG. S.1. Potential of Mean Force profiles considered in the simulations.

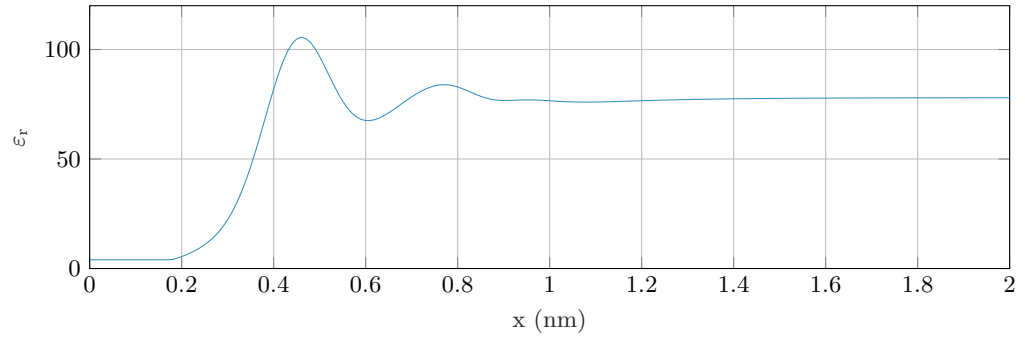

FIG. S.2. Profile of the water permittivity near the interface for two types of interfaces.

the PBS and is included as an additive component. The reactions involved in the pH regulation are the following ones:

$$\mathrm{H_3PO_4} \overset{pK'_{a_1,T}}{\rightleftharpoons} \mathrm{H^+} + \mathrm{H_2PO_4^-} \tag{4}$$

$$\mathrm{H_2PO_4^-} \overset{pK'_{a_2,T}}{\rightleftharpoons} \mathrm{H^+} + \mathrm{HPO_4^{2-}} \tag{5}$$

$$\mathrm{HPO_4^{2-}} \overset{pK'_{a_3,T}}{\rightleftharpoons} \mathrm{H^+} + \mathrm{PO_4^{3-}} \tag{6}$$

where $pK'_{a_i,T}$ are the temperature-dependent reaction constants. These values depend on the ionic strength I that is evaluated locally (in each point of the grid). So that, a local value of the reaction constants is obtained using the expressions:

$$\begin{cases} pK'_{a_i,T} = pK_{a_i,T} + (2z_{a_i} - 1)\left[\frac{A\sqrt{I}}{1+\sqrt{I}} - 0.1I\right] \\ pK_{a_i,T} = pK_{a_i} + \frac{dpK_{a_i}}{dT}(T - 298.15K) \end{cases} \tag{7}$$

where A is a temperature-dependent constant, z_{a_i} the charge of the conjugate acid species and pK_{a_i} is the reaction constant at $T = 298.15K$. The concentration of $\mathrm{H_2PO_4^-}$, $\mathrm{HPO_4^{2-}}$ and $\mathrm{PO_4^{3-}}$ can be calculated from the reactions described by expressions (4) to (6):

$$\left[\mathrm{H_2PO_4^-}\right] = \left[\mathrm{H_3PO_4}\right] 10^{pH - pK'_{a_1,T}} \tag{8}$$

$$\left[\mathrm{HPO_4^{2-}}\right] = \left[\mathrm{H_2PO_4^-}\right] 10^{pH - pK'_{a_2,T}} \tag{9}$$

$$\left[\mathrm{PO_4^{3-}}\right] = \left[\mathrm{HPO_4^{2-}}\right] 10^{pH - pK'_{a_3,T}} \tag{10}$$

The concentration $[\mathrm{H_3PO_4}]$ is the only value missed in this calculus, however, the sum of all the components of these reactions ($[\mathrm{H_3PO_4}]$, $\left[\mathrm{H_2PO_4^-}\right]$, $\left[\mathrm{HPO_4^{2-}}\right]$ and $\left[\mathrm{PO_4^{3-}}\right]$) has to be equal to the concentration of PBS:

Parameter	Value	Units
$pK_{a_1}\,(25^\circ C)$	2.15	
$pK_{a_2}\,(25^\circ C)$	7.21	
$pK_{a_3}\,(25^\circ C)$	12.33	
dpK_{a_1}/dT	0.0044	K^{-1}
dpK_{a_2}/dT	-0.0028	K^{-1}
dpK_{a_3}/dT	-0.026	K^{-1}
z_{a_1}	0	
z_{a_2}	-1	
z_{a_3}	-2	
A $(25^\circ C)$	0.5114	

TABLE I. Values used in the evaluation of $pK_{a_i,T}$, which are extracted from[8].

$$[\mathrm{H_3PO_4}] + \left[\mathrm{H_2PO_4^-}\right] + \left[\mathrm{HPO_4^{2-}}\right] + \left[\mathrm{PO_4^{3-}}\right] = [\mathrm{PBS}] \tag{11}$$

Therefore, the concentration of H_3PO_4 can be calculated as

$$[\mathrm{H_3PO_4}] = \frac{[\mathrm{PBS}]}{1 + 10^{pH - pK'_{a_1,T}}\left(1 + 10^{pH - pK'_{a_2,T}}\left(1 + 10^{pH - pK'_{a_3,T}}\right)\right)} \tag{12}$$

As we considered a PBS based on $NaH_2PO_4^-$ there is also a contribution to the sodium ion concentration:

$$\left[\mathrm{N_a^+}\right] = -z_{H_2PO_4^-}\left[\mathrm{H_2PO_4^-}\right] - z_{HPO_4^{2-}}\left[\mathrm{HPO_4^{2-}}\right] - z_{PO_4^{3-}}\left[\mathrm{PO_4^{3-}}\right] \tag{13}$$

All the parameters required for the calculation of the reaction constants $pK'_{a_i,T}$ are extracted from[8] and summarised in Table I. The electrolyte considered is a 1×PBS the composition of which is [NaCl] = 140mM, [KCl] = 2.7mM and $[NaH_2PO_4]$ = 10mM.

In addition to the charge associated to ions in the solution, we need to include the charge provided by the receptor molecules. We described the protein structures in atomic detail and assigned a partial charge to each atom using the PDB2PQR protocol[9]. This protocol includes protonation of the protein structures in order to optimize the hydrogen-bond network based on an empirical pKa estimation for titratable residues. The charges were assigned using the default PARSE force field parameters[10,11]. This task is performed in a three-dimensional (3D) description, so we need to translate this information to a 2D description in order to integrate it into the device level simulation. Figure S.3 schematically describes the procedure. We start with the 3D molecular charge profile and project it into a plane that is defined by the desired orientation for the molecule. This plane is discretized in agreement with the grid that will be later used in the device simulation so to achieve a straightforward insertion of the molecular charge.

SUPPORTING NOTE 2: MINORITY CARRIER CONCENTRATION UNDER RECEPTORS

Figure S.4 depicts the minority carrier concentration corresponding to two gate biases (V_{FG}), electrons in the p-branch (-0.5V) and holes in the n-branch (0.5V). The behavior of these profiles mimics that of the main carriers, analyzed in the main text. Beginning with electrons (Figure S.4a), they show a tightening of the region where their concentration decreases and, as a consequence, a more steep profile. In the case of holes (Figure S.4b), they depict a quite large increase (around ×3) when compared with the profile obtained for the p-branch (around ×1.5), although the magnitude of the charge in this latter scenario is much greater.

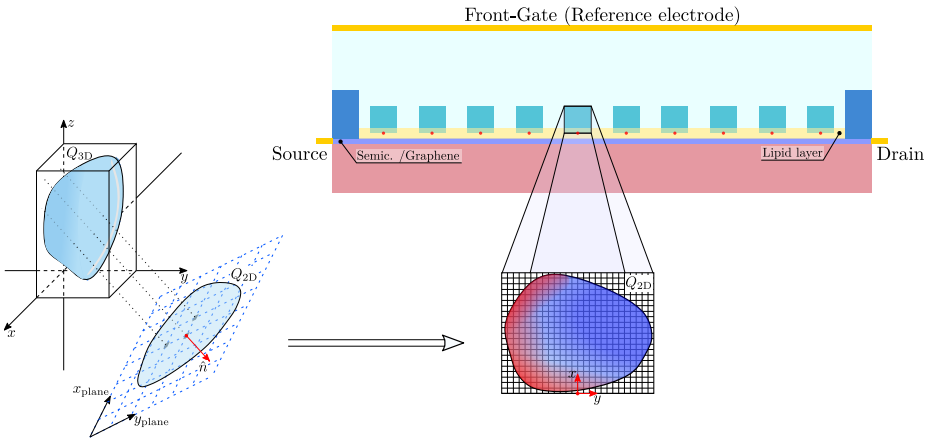

FIG. S.3. Projection of the 3D molecule charge distribution to obtain the 2D profiles used in the device simulation. Vector $\hat{n}$ sets the desired orientation for the projection plane that is later discretized to define the 2D charge profiles of the molecules. The extracted profiles are used in the device simulations by replicating them along the longitudinal axis according to the defined positions.

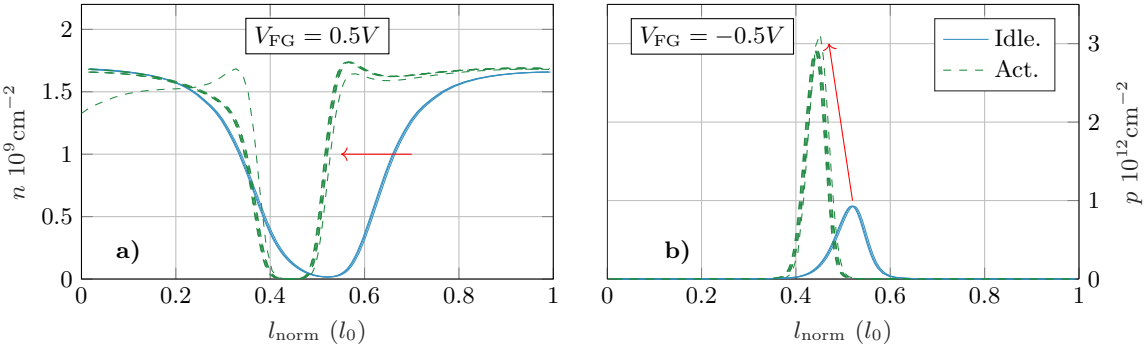

FIG. S.4. Superimposed minority carrier concentrations, that is, electrons in the p-branch (left) and holes in the n-branch (right), under each receptor. We consider a region of length l_0 under each receptor and $\alpha = 0.6$ (6 receptors are activated) to observe the changes in the carrier concentrations when the receptor is activated. The profiles behave in the same way as those for the majority carriers does, electron concentration drops under the molecule wile holes concentration increases. The latter is the one with the most remarkable behavior as hole concentration in the n-branch changes in a larger extent than in the p-branch.

SUPPORTING NOTE 3: MOLECULE - ELECTROLYTE MODEL VALIDATION

Aiming at the validation of our numerical approach, we have considered the work by Lud *et al.*[12] which addresses the detection of peptides and proteins by a thin-film resistor. More specifically, we have focused on the results given for the detection of aspartic acid. The fabricated structure is quite large (80μm×80μm), but, in contrast to most of references, their measurements are based on the surface potential which enables the analysis in a reduced structure (as long as the aspect ratio is kept) making it suitable to be reproduced and thus employed to validate the calculations at the molecule model level. To this end, the experimental structure considered for the simulations is depicted in Figure S.5a.

Figure S.5a shows the simulated structure, reproducing the experimental realization: a 30 nm-thick Si layer sandwiched in between two SiO_2 layers, a 20 nm-thick substrate and a 2 nm-thick cover. The latter is coated by the 1.5 nm-thick lipid layer that hosts the NTA headgroups that act as a receptors and has a -1q charge.

We first computed the profile of the surface potential as a function of the number of aspartic acid units considered in the histidine-aspartic acid complex attached to the receptors, and compared it with the experimental results provided by Lud *et al.* This profile is obtained for two Debye lengths κ^{-1} of the electrolyte, assuming 0.1xPBS solution with different KCl concentrations. For the modelling of the complex, histidine tag is considered electrically neutral, while each aspartic acid unit has a net charge of -1q. Their sizes are set according to the data provided in[12] and[13] for these two Debye legnths. The results depicted in Figure S.5b ($\kappa^{-1} = 1.1$ nm) and Figure S.5c ($\kappa^{-1} = 0.7$ nm), demonstrate that numerical simulations reproduce to a very good agreement the behaviour of the experimental data provided by[12]. The trend of the surface potential as a function of the number of aspartic

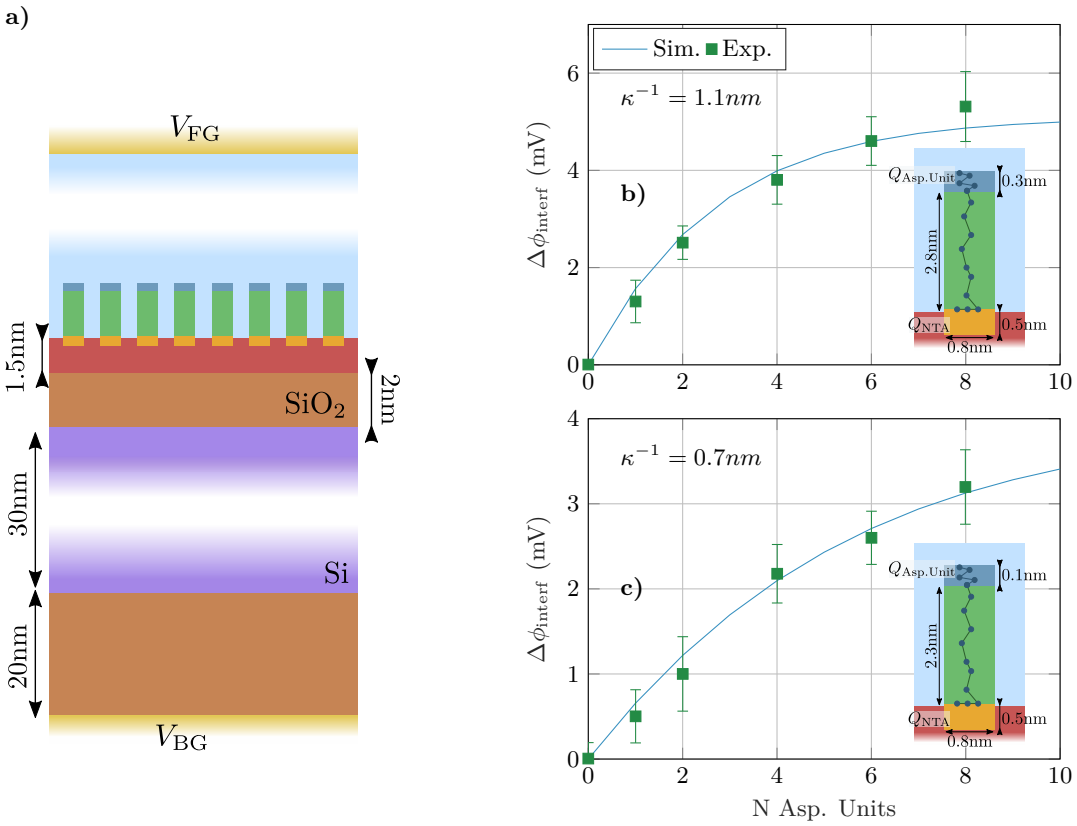

FIG. S.5. a) Structure used in the simulations for the validation against the experimental data from[12]. The material stack, from bottom to top, comprises: a SiO_2 substrate (20 nm-thick), a 30 nm-thick Si layer, and an additional 2 nm-thick SiO_2 layer. On top of the latter, a 1.5 nm-thick lipid layer hosts the NTA headgroup receptors, which has a net charge of -1q. The results obtained with our computational tool for the histidine-aspartic acid sample are compared with the experimental results in figures b) and c). There the change in the surface potential is plotted as a function of the number of aspartic acid units attached to the histidine tag for two different Debye lengths (κ^{-1}).

acid units is accurately replicated by the simulations for the two Debye lengths (ion concentrations) considered.

The validation is extended to fit the values provided in the same work for the Green Fluorescent Protein (GFP). The same structure as in Figure S.5a but changeing the molecule parameters to fit those for the GFP molecule: a 4 nm-height and 3nm-width block[13] with a net charge of -8q. The data provided for this case corresponds to the change in the surface potential as a function of the protein concetration in the sample. This requires an additional step to transpate the protein concentration c_{GPF} into number of activated receptor, which is the value considered in the simulations. This is done using the association constant extracted from the Langmuir isotherm fitting carried out in the paper:

$$N_{act} = N_{rec}\frac{K_d c_{GPF}}{1 + K_d c_{GPF}} \Rightarrow c_{GFP} = \frac{1}{K_d}\frac{1}{\frac{N_{rec}}{N_{act}} - 1} \tag{14}$$

where N_{rec} is the total number of receptor sites and N_{act} the number of activated sites. These two expressions make possible to translate between N_{act} and c_{GFP} using the K_d provided ($6.5{\cdot}10^5 M^{-1}$) and the number of receptor sites in the simulation ($N_{rec} = 10$). The result of these simulations are depicted in Figure S.6.

It is worth to highlight that this validation, at the molecule-charge and sensor-surface potential levels, is the most relevant to demonstrate the capability of the computational approach proposed here, i.e. the possibility to treat, in a multiscale fashion, the details about the molecular properties into a complete device level study. This validation is, indeed, complementary to those others of the electrolyte ions interaction[14] and the semiconductor[15] that we already accomplished in less sophisticated versions of the implemented tool and with other purposes.

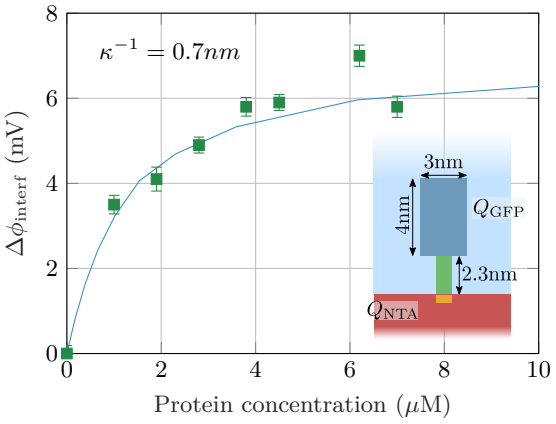

FIG. S.6. Change of the surface potential as a function of the protein concetraiton in the sample. The structure considered is the same as the one depiected in Figure S.5a but using the Green Fluorescent Protiein (GFP) instead of aspartic acid, which depicts a higer net charge (-8q) and size (4 nm×3 nm).

[1] James G. Champlain. A first principles theoretical examination of graphene-based field effect transistors. *Journal of Applied Physics*, 109(8):084515, apr 2011.

[2] Farhan Rana, Paul A. George, Jared H. Strait, Jahan Dawlaty, Shriram Shivaraman, Mvs Chandrashekhar, and Michael G. Spencer. Carrier recombination and generation rates for intravalley and intervalley phonon scattering in graphene. *Physical Review B*, 79(11), mar 2009.

[3] Jahan M. Dawlaty, Shriram Shivaraman, Mvs Chandrashekhar, Farhan Rana, and Michael G. Spencer. Measurement of ultrafast carrier dynamics in epitaxial graphene. *Applied Physics Letters*, 92(4):042116, jan 2008.

[4] Pedro C Feijoo, David Jiménez, and Xavier Cartoixà. Short channel effects in graphene-based field effect transistors targeting radio-frequency applications. *2D Materials*, 3(2):025036, jun 2016.

[5] Itamar Borukhov, David Andelman, and Henri Orland. Steric effects in electrolytes: A modified Poisson-Boltzmann equation. *Physical Review Letters*, 79(3):435–438, jul 1997.

[6] Nadine Schwierz, Dominik Horinek, and Roland R. Netz. Reversed anionic hofmeister series: The interplay of surface charge and surface polarity. *Langmuir*, 26(10):7370–7379, may 2010.

[7] Nadine Schwierz, Dominik Horinek, and Roland R. Netz. Anionic and cationic hofmeister effects on hydrophobic and hydrophilic surfaces. *Langmuir*, 29(8):2602–2614, feb 2013.

[8] Stefan Birner. *Modeling of semiconductor nanostructures and semiconductor–electrolyte interfaces*. PhD thesis, Technische Universität München, 2011.

[9] T. J. Dolinsky, P. Czodrowski, H. Li, J. E. Nielsen, J. H. Jensen, G. Klebe, and N. A. Baker. PDB2pqr: expanding and upgrading automated preparation of biomolecular structures for molecular simulations. *Nucleic Acids Research*, 35(Web Server):W522–W525, may 2007.

[10] Doree Sitkoff, Kim A. Sharp, and Barry Honig. Accurate calculation of hydration free energies using macroscopic solvent models. *The Journal of Physical Chemistry*, 98(7):1978–1988, feb 1994.

[11] Christopher L. Tang, Emil Alexov, Anna Marie Pyle, and Barry Honig. Calculation of pKas in RNA: On the structural origins and functional roles of protonated nucleotides. *Journal of Molecular Biology*, 366(5):1475–1496, mar 2007.

[12] Simon Q. Lud, Michael G. Nikolaides, Ilka Haase, Markus Fischer, and Andreas R. Bausch. Field effect of screened charges: Electrical detection of peptides and proteins by a thin-film resistor. *ChemPhysChem*, 7(2):379–384, jan 2006.

[13] S Birner, C Uhl, M Bayer, and P Vogl. Theoretical model for the detection of charged proteins with a silicon-on-insulator sensor. *Journal of Physics: Conference Series*, 107:012002, mar 2008.

[14] A. Toral-Lopez, E. G. Marin, J. M. Gonzalez-Medina, F. J. Romero, F. G. Ruiz, D. P. Morales, N. Rodriguez, and A. Godoy. Assessment of three electrolyte–molecule electrostatic interaction models for 2D material based BioFETs. *Nanoscale Advances*, 1(3):1077–1085, 2019.

[15] Alejandro Toral-Lopez, Francisco Pasadas, Enrique G. Marin, Alberto Medina-Rull, Jose Maria Gonzalez-Medina, Francisco J Garcia Ruiz, David Jiménez, and Andres Godoy. Multi-scale analysis of radio-frequency performance of 2D-material based field-effect transistors. *Nanoscale Advances*, 3(8):2377–2382, 2021.